Earth and Planetary Science Letters 452 (2016) 69–78

Contents lists available at ScienceDirect

Earth and Planetary Science Letters

www.elsevier.com/locate/epsl

Manganese oxide shuttling in pre-GOE oceans – evidence from molybdenum and iron isotopes

Florian Kurzweil [a,b,*], Martin Wille [a], Niklas Gantert [a], Nicolas J. Beukes [c], Ronny Schoenberg [a]

[a] Eberhard Karls University of Tuebingen, Department of Geosciences, Wilhelmstraße 56, 72074 Tuebingen, Germany
[b] University of Cologne, Department of Geosciences, Greinstraße 4-6, 50939 Cologne, Germany
[c] CIMERA and PPM, Department of Geology, University of Johannesburg, P.O. Box 524, Auckland Park 2006, South Africa

ARTICLE INFO

Article history:
Received 18 March 2016
Received in revised form 7 July 2016
Accepted 8 July 2016
Available online 8 August 2016
Editor: D. Vance

Keywords:
Great Oxidation Event
Mo isotopes
Fe isotopes
oxygen oases
redox stratification
Koegas Subgroup

ABSTRACT

The local occurrence of oxygen-rich shallow marine water environments has been suggested to significantly predate atmospheric oxygenation, which occurred during the Great Oxidation Event (GOE) ca. 2.4 billion years ago. However, the potential influence of such 'oxygen oases' on the mobility, distribution and isotopic composition of redox sensitive elements remains poorly understood. Here, we provide new molybdenum and iron isotopic data from shallow marine carbonate and silicate iron formations of the Koegas Subgroup, South Africa, that confirm local ocean redox stratification prior to the GOE.

Mn concentrations correlate negatively with both δ^{98}Mo and δ^{56}Fe values, which highlights the substantial role of particulate manganese for the cycling of Mo and Fe in the Paleoproterozoic oceans. Based on these trends we propose that pore water molybdate was recharged (1) by the diffusional transport of seawater molybdate with high δ^{98}Mo and (2) by the re-liberation of adsorbed molybdate with low δ^{98}Mo during Mn oxide dissolution within the sediment. The relative contribution of isotopically light Mo is highest close to a Mn chemocline, where the flux of Mn oxides is largest, causing the negative correlation of Mn concentrations and δ^{98}Mo values in the Koegas sediments. The negative correlation between δ^{56}Fe values and Mn concentrations is likely related to Fe isotope fractionation during Fe(II) oxidation by Mn oxides, resulting in lower δ^{56}Fe values in the uppermost water column close to a Mn chemocline. We argue that the preservation of these signals within Paleoproterozoic sediments implies the existence of vertically extended chemoclines with a smoother gradient, probably as a result of low atmospheric oxygen concentrations. Furthermore, we suggest that abiotic oxidation of Fe(II) by a Mn oxide particle shuttle might have promoted the deposition of the Koegas iron formations.

1. Introduction

The GOE, between 2.45 and 2.32 billion years (Ga) ago, represents one of the major environmental changes in Earth history (Holland, 2006). During this time period the amount of atmospheric oxygen rose from below 10^{-5} up to 10^{-2} of its present level (Farquhar et al., 2000; Holland, 2006; Pavlov and Kasting, 2002). This leap in atmospheric oxygen concentration most likely reflects a combination of increased primary production by oxygenic photosynthesis and organic carbon burial, a decrease in the O_2 buffer capacity of the Earth's crust, hydrosphere and atmosphere or a combination of both (Catling et al., 2001; Holland, 2006; Kump and Barley, 2007).

There are several lines of evidence, which suggest that the onset of oxygen production occurred several hundred million years before the GOE and was most likely of biogenic origin (Kendall et al., 2010; Kurzweil et al., 2013; Planavsky et al., 2014). However, the reducing power of the upper continental crust, the atmosphere and the deep ocean outbalanced oxygen production and prevented the earlier accumulation of free oxygen (Lyons et al., 2014). Separated from anoxic deep waters, only some shallow marine habitats became oxygenated (Olson et al., 2013), which caused the development of a locally stratified ocean margin (Kendall et al., 2010). The existence of such oxygen oases is indicated by various geochemical parameters such as transition metal abundances (Kendall et al., 2010), Mo–Fe isotope constraints (Czaja et al., 2012; Planavsky et al., 2014), and the coupling of S and C isotopes

* Corresponding author. Present address: University of Cologne, Institute for Geology and Mineralogy, Zülpicher Straße 49b, 50674 Cologne, Germany. Fax: +49 707129571.
E-mail address: flokurzweil@hotmail.de (F. Kurzweil).

http://dx.doi.org/10.1016/j.epsl.2016.07.013
0012-821X/

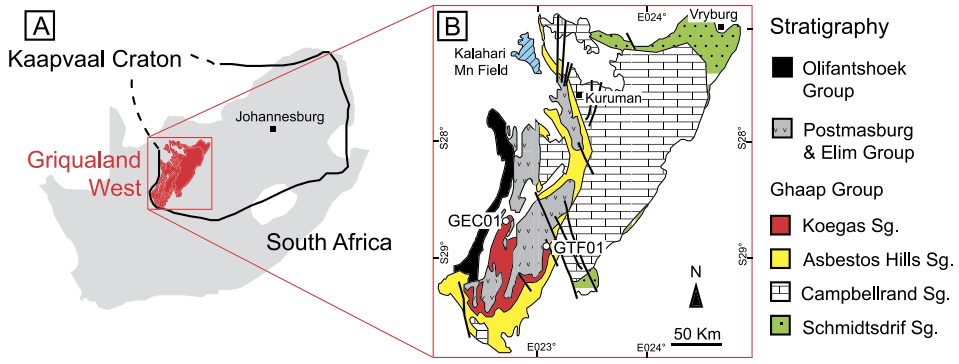

Fig. 1. A: Location of the Griqualand West Basin on the Kaapvaal Craton, South Africa (modified from Schröder et al., 2011). B: Geological map of the Griqualand West Basin and the location of drill cores of GEC01 and GTF01 (modified from Schröder et al., 2011).

(Kaufman et al., 2007). However, the temporal and spatial extension of oxygen oases and the implications for the local and global isotopic composition of different redox sensitive elements remain poorly understood.

Iron isotopes can potentially be used to reconstruct the ancient marine redox-state (Rouxel et al., 2005) because the redox dependent speciation of iron is accompanied by fractionation processes. Dissolved $Fe(II)_{aq}$ and poorly soluble $Fe(III)_{aq}$ isotopically equilibrate within minutes, with a large isotopic difference of $\Delta^{56}Fe_{FeII-FeIII} = \delta^{56}Fe_{FeII} - \delta^{56}Fe_{FeIII} = -3‰$ (Welch et al., 2003), which is largely independent of the exact oxidation pathway (e.g. abiotic oxidation with O_2 or biological oxidation by anoxygenic photoferrotrophs (Croal et al., 2004)). The subsequent precipitation of $Fe(III)_{aq}$ as Fe-oxyhydroxide minerals causes a kinetic isotope fractionation in the opposite direction, the magnitude being mainly dependent on the mineral species, temperature and reaction kinetics (Beard and Johnson, 2004). For zero age ferrihydrite the isotopic difference is $\Delta^{56}Fe_{FeIII-FeOOH} = \delta^{56}Fe_{FeIII} - \delta^{56}Fe_{FeOOH} = +2‰$ (Beard and Johnson, 2004; Johnson et al., 2008b). Altogether the oxidation and precipitation of Fe(III) minerals cause the relative depletion of heavy Fe isotopes in the remaining $Fe(II)_{aq}$ reservoir. The separation of anoxic $Fe(II)_{aq}$-rich deep waters with a homogeneous isotopic composition and an oxic surface layer, where $Fe(II)_{aq}$ is oxidized, therefore causes large isotopic gradients along the chemocline (Busigny et al., 2014). The Fe isotopic composition of sediments deposited along such chemoclines, thus, potentially records redox gradients at ancient local oxygen oases.

In contrast to Fe, Mo is poorly reactive in oxic, and probably also in anoxic-ferruginous, waters (Kurzweil et al., 2015). In the modern predominantly oxic ocean dissolved molybdate (MoO_4^{2-}) has a residence time of around 440 ka (Miller et al., 2011) and is, therefore, homogeneously distributed in concentration as well as in its isotopic composition (Nakagawa et al., 2012; Siebert et al., 2003). In the absence of dissolved H_2S, the adsorption of Mo onto Mn-oxides probably represents the most important Mo sink in oxic deep marine settings (Bertine and Turekian, 1973; Scott and Lyons, 2012). This adsorption is associated with a change from tetrahedral (MoO_4^{2-}) to octahedral coordination (adsorbed Mo), which causes large equilibrium Mo isotopic fractionation, thereby preferentially adsorbing light Mo isotopes (Barling and Anbar, 2004; Kashiwabara et al., 2011; Siebert et al., 2003).

The oxidation of Mn(II) and the formation of Mn oxides requires higher redox potentials than the oxidation of Fe(II) as well as the catalyzing effect of Mn oxidizing bacteria (Tebo et al., 2005). Reaction kinetics are accelerated in the presence of superoxide (O_2^-), which can be produced during biological processes or photochemical reactions, such as the photo-oxidation of dissolved organic matter (Learman et al., 2013). In an overall reducing ocean, shallow ocean environments with high primary productivity, therefore, represent the most likely setting, where the required availability of O_2 and/or O_2^- enables the formation of particulate Mn oxides. In these most proximal, shallow ocean areas the preferential scavenging of isotopically light Mo by Mn oxide particles is expected at Archean/Paleoproterozoic times (Planavsky et al., 2014). The combination of Fe and Mo isotopes from shallow marine, Superior type iron formations of the 2.48 Ga old Koegas Subgroup, South Africa, therefore offer great potential for the detailed reconstruction of the local environmental redox state of the Griqualand West Basin. We compare our results with isotopic data for modern anoxic lakes, which have been claimed as Archean ocean analogues (Busigny et al., 2014), as well as isotopic data for sediments from other oxygen oases (Planavsky et al., 2014). Furthermore, the combination of Mo and Fe isotopes in our study not only provides important insights into the local marine environment, with profound implications for the regional/global ocean redox state, but also constraints on the behavior of redox sensitive elements like Mo and Fe in such settings in general.

2. Geological setting and sample material

The Ghaap Group (Traansvaal Supergroup, South Africa) represents a continuous sedimentary succession, deposited in the Griqualand West Basin immediately before the GOE (Beukes and Gutzmer, 2008). The Koegas Subgroup is the uppermost unit of the Ghaap Group and represents the final stage of a long-term regressive period (Schröder et al., 2011). SHRIMP U–Pb zircon data of the subjacent Asbestheuwels Subgroup (Kuruman Formation) indicate a maximum depositional age of 2460 ± 5 Ma (Pickard, 2003). In contrast, Re–Os dating of shales from the Koegas Subgroup (Nelani Formation, Klipputs Member; GEC01 174–176) provide a depositional age of 2479 ± 22 Ma (Kendall et al., 2013), which might suggest a true depositional age at the lower end of this error range.

Shorter term sea level fluctuations are superimposed on the long-term regressive period, leading to periodical alternations of siliciclastic units during regressions (Pannetjie-, Naragas-, Heynskop Formation) and iron formations during transgressions (Doradale-, Rooinekke-, Nelani Formation) along a prograding delta or submarine fan system (Schröder et al., 2011). The terrigenous input was generally higher in the eastern parts of the basin, which argues for lateral basinal deepening from E to W (Schröder et al., 2011). The drillcore GTF01 situated in the eastern part of the basin therefore represents a more proximal depositional setting (Fig. 1). GTF01 samples of this study are from the Doradale Formation, which is associated with maximal sea level and the deposition of fine-grained and laminated iron formations. The western GEC01 drillcore comprises sediments from the deeper settings of the Rooinekke and Nelani formations. Beukes (1983) suggested a flooding surface at the base of the Nelani Formation during deposition

of the Klipputs Member. The subsequent regression during the Nelani Formation ends in granular carbonate iron formations (sample GEC 65.9), which represent deposition above wave base.

The petrological and mineralogical composition of our samples is described in detail by Nel (2013). This author mainly distinguishes between Fe-carbonate lutite and Fe-silicate lutite dominated samples, as well as a combination of both. In most samples dark green-black, very fine grained and massive Fe-silicate lutite layers alternate with lighter colored, greyish Fe-carbonate lutite layers. The latter are coarser grained and can form a peloidal structure. This alternation results in fine laminations visible on the core material (Nel, 2013). The abundance of Fe-oxides (mainly magnetite) is minor compared to Fe-silicates (stilpnomelane and greenalite) and Fe-carbonates (siderite and ankerite) (Nel, 2013). A few samples have minor riebeckite (Table 1), which points to low-grade metamorphism of the Koegas Subroup (Schröder et al., 2011). Pyrite is abundant in detrital form in sandstone units of the Koegas Subgroup and as a late diagenetic phase in shaly successions (J.E. Johnson et al., 2013). Within our studied iron formation pyrites are absent (Nel, 2013). Very low concentrations of Al_2O_3 in our samples strongly suggest that the terrigenous input was low (Table S1).

3. Methods

For Fe isotope measurements ~20 mg of powdered sample material were digested at 120 °C for 48 h using a 3:1 mixture of distilled HF and HNO_3 acids. Subsequently, dried samples were redissolved and dried twice in distilled 6 M HCl, assuring complete dissolution of fluoride compounds, and finally taken up in 3 ml of 6 M HCl. An aliquot containing around 30 µg Fe was split for further purification of Fe. The separation of Fe by the use of an anion exchange resin (AG1-X8, 100–200 mesh) follows a procedure described by Schoenberg and von Blanckenburg (2005).

Purified samples were dissolved in 0.3 M HNO_3 and introduced into a multi collector ICP-MS (ThermoFisher Scientific Neptune-Plus; University of Tuebinga) using a dual spray chamber system with a PFA pneumatic nebulizer. Isotopic ratios were measured at high resolution, which assured the resolution of polyatomic interferences such as $^{40}Ar^{16}O^+$ on $^{56}Fe^+$ and $^{40}Ar^{14}N^+$ on $^{54}Fe^+$ (Weyer and Schwieters, 2003). The isobaric interferences from $^{54}Cr^+$ and $^{58}Ni^+$ were corrected for by simultaneous measurements of $^{52}Cr^+$ and $^{60}Ni^+$, respectively, and the use of published relative isotope abundance data (de Laeter et al., 2003) and assuming the same instrumental mass bias for Cr and Ni as determined for Fe. Fe isotopic ratios were measured using the standard-sample bracketing method (Schoenberg and von Blanckenburg, 2005). Each sample measurement was bracketed by IRMM-014 reference solution measurements (Institute of Reference Material and Measurements, Geel, Belgium). Measurements consisted of 20 integration cycles of 8.4 s each. Fe isotopic ratios are presented in the δ-notation and relative to the reference solution of IRMM-014 and are expressed in ‰ by multiplication by 1000:

$$\delta^{56}\mathrm{Fe} = \left(\frac{(\frac{^{56}\mathrm{Fe}}{^{54}\mathrm{Fe}})_{\mathrm{Sample}}}{(\frac{^{56}\mathrm{Fe}}{^{54}\mathrm{Fe}})_{\mathrm{IRMM\text{-}014}}} - 1 \right)$$

All samples were measured twice and average isotopic values are presented in Table 1. The long-term reproducibility of the in-house HanFe standard is 0.287 ± 0.055‰ (2SD; $n = 145$). Aliquots of the HanFe standard were measured during the course of this study, showing average δ^{56}Fe values of 0.294 ± 0.039‰ (2SD, $n = 11$), which is also consistent with published values (Moeller et al., 2014). The IF-G reference material, a banded iron formation from Isua, Greenland, which went through all purification steps in the course of this study, shows a δ^{56}Fe value of 0.644‰, which is also in agreement with literature values (Dauphas and Rouxel, 2006). The corrections for isobaric Cr and Ni interferences were always lower than 0.008‰ in δ^{56}Fe values and 0.7‰ in δ^{58}Fe values, respectively. Total chemical procedural blanks were ~4 ng Fe, contributing less than 0.1% to the amount of processed sample iron, which is negligible and was, thus, not corrected.

For Mo isotope measurements 100–300 mg of powdered and ashed (12 h at 600 °C) sample material, equivalent to ~50 ng Mo, was mixed with a ^{97}Mo–^{100}Mo double spike and digested using the dissolution method described above. The double spike method allows the correction of mass dependent isotope fractionations induced by the chemical purification of the target element and produced by the mass spectrometer during isotope analyses. Chemical purification of Mo was achieved using a combination of anion and cation exchange resins (Eichrom AG1-X8, 200–400 mesh; Eichrom 50WX8, 200–400 mesh).

Mo isotopic ratios were measured in low resolution mode with the multi collector ICP-MS at the University of Tuebinga using a CETAC Aridus II^{TM} desolvating nebulizer sample introduction system. The isobaric interferences of $^{96}Ru^+$, $^{98}Ru^+$, and $^{100}Ru^+$ were corrected for by simultaneous measurements of $^{99}Ru^+$ and the use of published relative isotope abundance data (de Laeter et al., 2003), assuming the same instrumental mass bias for Ru as determined for Mo. Acid blank analyses, which bracketed each sample and standard measurement, were used for an on-peak-zero baseline subtraction. Samples and standards were measured for 100 cycles, each having an integration time of 8.4 s. The Mo isotopic data are reported in the δ-notation relative to NIST 3134 and expressed in ‰ by multiplication with 1000:

$$\delta^{98}\mathrm{Mo} = \left(\frac{(\frac{^{98}\mathrm{Mo}}{^{95}\mathrm{Mo}})_{\mathrm{Sample}}}{(\frac{^{98}\mathrm{Mo}}{^{95}\mathrm{Mo}})_{\mathrm{NIST3134}}} - 1 \right)$$

Thereby, NIST3134 was set to +0.25‰ for better comparison with earlier published data (Nägler et al., 2014). The repeated cross-calibration of NIST 3134 with our in-house standard Johnson Matthey ICP during the measurement sequence of this study showed an isotopic difference of $\Delta^{98}\mathrm{Mo}_{\mathrm{NIST3134\text{-}JM}} = 0.286 \pm 0.030$‰ (2SD; $n = 4$), which is in agreement with the long term average $\Delta^{98}\mathrm{Mo}_{\mathrm{NIST3134\text{-}JM}}$ value of 0.273 ± 0.031‰ (2SD, $n = 32$) as well as with literature values (Goldberg et al., 2013; Greber et al., 2012). A second in-house standard, ZH-2, which ran through all purification steps during the course of this study shows a $\delta^{98}\mathrm{Mo}_{\mathrm{NIST\ 3134+0.25}}$ value of 1.001‰ and 0.970‰, respectively. These values are consistent with the long-term reproducibility of ZH-2, which is 0.995 ± 0.086‰ (2σ; $n = 16$) as well as with literature values (Lehmann et al., 2007). The correction for isobaric Ru interferences was always lower than 0.08‰ in δ^{98}Mo values. The total procedural blank of the purification chemistry was below 0.2 ng, which compared to the amount of processed sample Mo was regarded as negligible and, thus, no correction on the isotopic data was carried out.

4. Results

The Fe isotope results for the Koegas Subgroup sediments show distinct trends through the stratigraphic column (Fig. 2; Table 1). During the deposition of the Doradale and the Rooinekke formations δ^{56}Fe values decline from −0.75‰ to −1.82‰, immediately below the flooding event (Interval 1; GTF01 + GEC01 250–195 m). Further up in the stratigraphy, we observe a sharp increase in δ^{56}Fe values at the base of the Nelani Formation (Klipput-Member, Interval 2; GEC01 195–160 m) followed by a smooth decrease through the Nelani Formation from 0.41‰ to −0.93‰ (Interval 3 GEC 160–50 m; Fig. 2). Low δ^{56}Fe values during the iron formation

Table 1
Fe and Mo isotopic composition.

Formation	Drillcore/ depth	Depth (m)	Lithology	$\delta^{56/54}Fe_{IRMM-014}$ (‰)	2SE	$\delta^{57/54}Fe$ (‰)	2SE	$\delta^{58/54}Fe$ (‰)	2SE	$\delta^{57/56}Fe$ (‰)	2SE	Mo µg/g	$\delta^{98}Mo_{NIST\ 3134+0.25}$ (‰)	2SE	Mo µg/g	*Replicates*	
																$\delta^{98}Mo_{NIST\ 3134+0.25}$ (‰)	Mo µg/g
Nelani	**GEC 53.2**	53.2	sid	**−0.93**	0.08	−1.36	0.11	−1.94	0.42	−0.43	0.03	0.24	**0.48**	0.02	**0.20**	*0.48*	*0.21*
	GEC 65.9	65.9	sid (gr IF)	**−1.11**	0.03	−1.64	0.05	−1.73	0.37	−0.53	0.05	0.16	**0.46**	0.02	**0.16**		
	GEC 82.2	82.2	sid–sil	**−0.93**	0.03	−1.37	0.08	−1.89	0.02	−0.44	0.05	0.24	**0.96**	0.02	**0.27**	*1.09*	*0.24*
	GEC 82.8	82.8	sil–sid	**−0.49**	0.03	−0.74	0.08	−1.16	0.13	−0.25	0.05	0.63	**0.91**	0.02	**0.59**	*0.82*	*0.63*
	GEC 84	84	sid–sil	**−0.16**	0.03	−0.27	0.06	−0.24	0.44	−0.12	0.06	0.45	**1.03**	0.02	**0.46**	*1.02*	*0.45*
	GEC 87.5	87.5	mag sid–sil	**−0.55**	0.03	−0.81	0.07	−0.98	0.39	−0.27	0.06	0.28	**0.77**	0.02	**0.30**	*0.73*	*0.28*
	GEC 118	118	sid (rieb)	**−0.60**	0.03	−0.90	0.09	−1.09	0.13	−0.29	0.06	0.16	**0.52**	0.02	**0.16**		
	GEC 120	120		**−1.34**	0.01	−1.97	0.01	−2.56	0.03	−0.63	0.00	0.09	**0.44**	0.03	**0.09**		
	GEC 122.5	122.5	sid	**0.18**	0.02	0.25	0.00	0.32	0.08	0.07	0.02	0.15	**0.71**	0.02	**0.15**		
	GEC 126.5	126.5	sid (sil)	**−0.26**	0.03	−0.38	0.12	−0.38	0.08	−0.12	0.08	0.13	**0.67**	0.03	**0.13**		
	GEC 135.5	135.5	sid (rieb)	**−0.09**	0.04	−0.09	0.04	−0.22	0.11	0.00	0.00	0.15	**0.86**	0.04	**0.15**		
	GEC 140	140	sid (sil)	**0.04**	0.04	0.06	0.06	0.09	0.30	0.02	0.01	0.22	**0.66**	0.03	**0.22**		
	GEC 144.3	144.3	sil	**0.41**	0.04	0.57	0.03	0.78	0.07	0.16	0.01	0.24	**1.03**	0.02	**0.23**	*1.03*	*0.24*
	GEC 164.5	164.5	sil	**−0.09**	0.02	−0.14	0.00	−0.02	0.01	−0.05	0.02	0.60	**0.53**	0.02	**0.66**	*0.52*	*0.60*
	GEC 172.5	172.5	sid–sil	**0.06**	0.03	0.09	0.06	0.16	0.29	0.03	0.04	0.71	**0.50**	0.02	**0.85**	*0.47*	*0.71*
	GEC 181.1	181.1	sid–sil	**−0.48**	0.01	−0.71	0.05	−0.47	0.23	−0.23	0.06	0.07	**0.43**	0.02	**0.07**		
Rooinekke	**GEC 202.5**	202.5	sid–sil	**−1.82**	0.01	−2.67	0.03	−3.52	0.21	−0.86	0.03	0.09	**0.45**	0.05	**0.09**		
	GEC 209.4	209.4	sil	**−1.26**	0.02	−1.89	0.04	−2.23	0.29	−0.63	0.05	0.17	**0.32**	0.02	**0.17**	*0.29*	*0.17*
	GEC 231.7	231.7	sid–sil	**−1.27**	0.03	−1.88	0.03	−2.33	0.02	−0.61	0.00	0.50	**−0.01**	0.01	**0.50**		
	GEC 257	257	sil sid (rieb)	**−1.21**	0.03	−1.80	0.04	−2.31	0.19	−0.59	0.01	0.53	**0.11**	0.02	**0.53**	*0.09*	*0.52*
	GEC 259	259	sid–sil	**−1.30**	0.01	−1.92	0.01	−2.52	0.03	−0.62	0.01	0.17	**0.32**	0.04	**0.16**		
	GEC 284.7	284.7	sid–sil	**−1.09**	0.02	−1.63	0.10	−2.21	0.01	−0.54	0.08	0.40	**0.36**	0.02	**0.41**	*0.34*	*0.40*
Doradale	**GTF 248.5**	248.5	sid–sil	**−1.19**	0.02	−1.77	0.03	−2.24	0.25	−0.58	0.05	0.22	**0.48**	0.02	**0.22**	*0.49*	*0.22*
	GTF 251.5	251.5	sid–sil	**−0.79**	0.01	−1.18	0.02	−1.47	0.23	−0.39	0.03	0.52	**0.88**	0.01	**0.52**		
	GTF 257.3	257.3	sid–sil	**−1.23**	0.01	−1.83	0.01	−2.23	0.00	−0.60	0.01	0.73	**0.46**	0.02	**0.73**		
	GTF 263.4	263.4	sil–sid	**−1.07**	0.10	−1.58	0.13	−1.78	0.07	−0.51	0.03	0.39	**0.46**	0.01	**0.39**		
	GTF 266.8	266.8	sil–sid	**−0.94**	0.03	−1.34	0.08	−1.46	0.33	−0.40	0.06	0.29	**0.68**	0.02	**0.27**	*0.64*	*0.28*
	GTF 269.2	269.2	sid–sil	**−1.05**	0.01	−1.55	0.02	−1.73	0.02	−0.51	0.03	0.31	**0.51**	0.03	**0.21**	*0.62*	*0.31*
	GTF 278	278	sil–sid	**−0.75**	0.01	−1.14	0.02	−1.95	1.00	−0.39	0.01	0.95	**0.36**	0.02	**0.96**	*0.3*	*0.95*
	GTF 278.8	278.8	sil–sid	**−0.89**	0.03	−1.34	0.01	−1.75	0.02	−0.45	0.03	0.28	**0.25**	0.03	**0.29**	*0.26*	*0.28*

sil: Fe-silicate; sid: siderite; rieb: riebeckite; mag: magnetite; gr IF: granular iron formation.

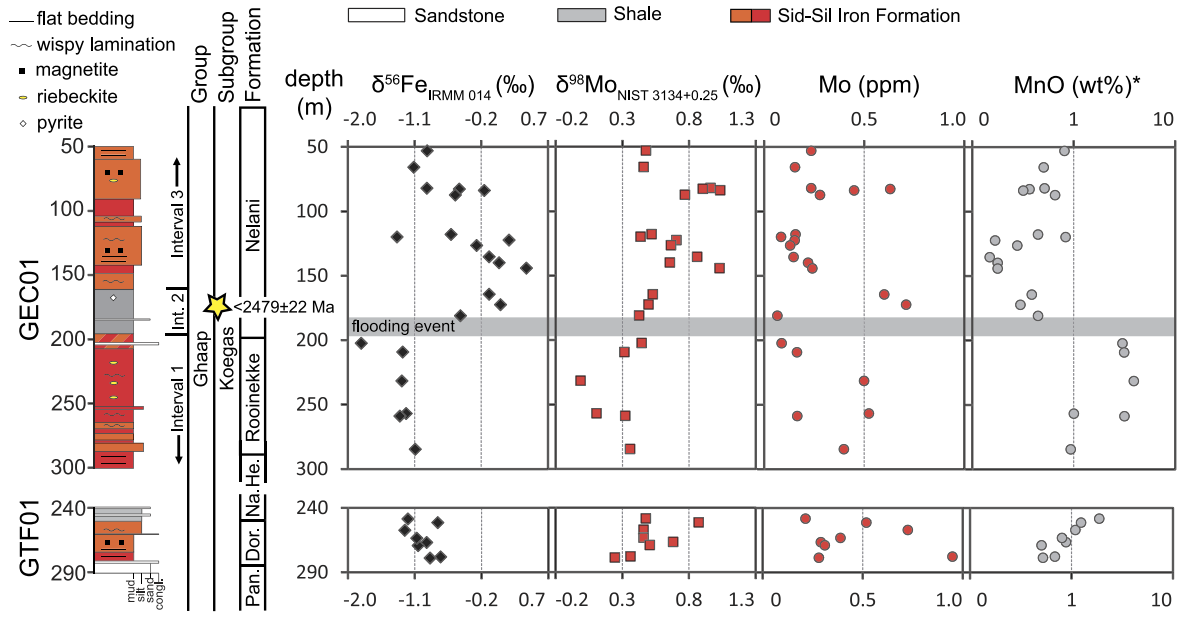

Fig. 2. Stratigraphic description of drill cores GEC01 and GTF01. Re–Os dating of shales deposited at the base of the Nelani Formation during the Klipputs Member provide a maximum depositional age of 2479 ± 22 Ma (Kendall et al., 2013). Selected geochemical parameters are shown against drill core depth. (* MnO concentrations are from Nel, 2013). Pan.: Pannetjie; Dor.: Doradale; Na.: Naragas; He: Heynskop.

dominated interval 1 are accompanied by relatively high Mn concentrations. The continuous sharp increase during interval 2 reflects a change in lithology from pure iron formations towards alternations of shaly sediments and silicate lutites. This change is also marked by higher Al concentrations and near crustal δ^{56}Fe values (Beard et al., 2003) in this interval. The iron formation dominated succession between 150 and 50 m again shows low Al concentrations (Table S1). However, these iron formations exhibit significantly lower Mn concentrations compared to the lower iron formation section. All intervals together show a negative correlation of δ^{56}Fe values with Mn concentrations (Fig. 3A). However, no correlation is observed between δ^{56}Fe values and Al_2O_3 concentrations (Fig. 4A).

The concentration of Mo varies between 0.07 and 0.95 ppm. We observe no correlation of Mo concentrations with the Mo and Fe isotopic compositions, respectively. Furthermore, correlations between Mo concentrations and Al_2O_3 and MnO abundances, respectively, are absent (Fig. 4B, C). Along the stratigraphic column δ^{98}Mo and δ^{56}Fe values follow similar trends, although the magnitude of Mo isotope variation is somewhat smaller (Fig. 2). We observe $\delta^{98}Mo_{NIST\ 3134+0.25}$ values between −0.01 and 0.88‰ during interval 1 (average of 0.40‰). The shaly succession of interval 2 shows $\delta^{98}Mo_{NIST\ 3134+0.25}$ values around 0.43 and 0.55‰, which is close to the expected range for the detrital Mo isotopic composition (Voegelin et al., 2014). The uppermost interval 3 includes the heaviest Mo isotope ratios of the whole sample set, with $\delta^{98}Mo_{NIST\ 3134+0.25}$ values ranging between 0.44 and 1.03‰ (average of 0.73‰). Like δ^{56}Fe values, δ^{98}Mo values correlate negatively with Mn concentrations (Fig. 3B), although this correlation is less pronounced.

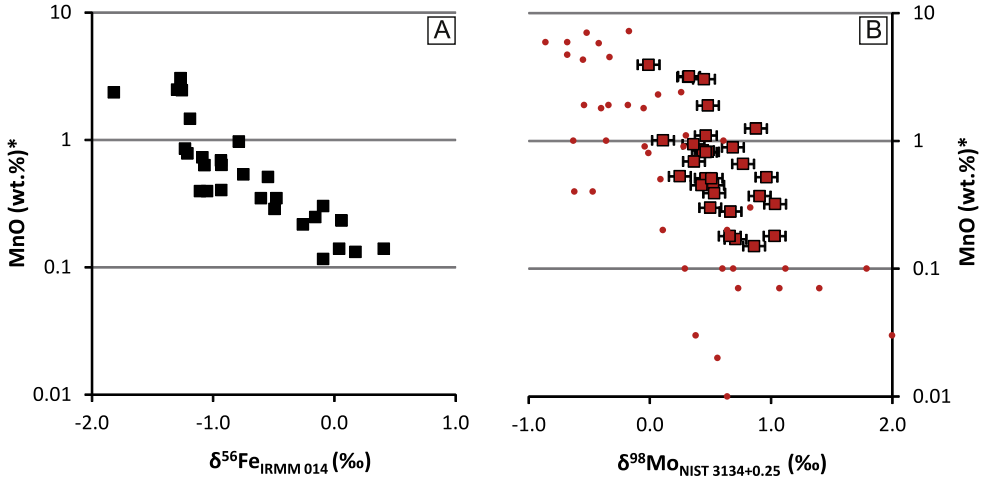

Fig. 3. A) δ^{56}Fe values show a negative correlation with MnO* concentrations (* from Nel, 2013), which could result from Fe(II) oxidation by Mn oxides and the accompanying depletion of heavy Fe isotopes in the uppermost water column. B) The negative correlation of δ^{98}Mo values and MnO concentration in Precambrian banded iron formations (red dots: Planavsky et al., 2014; red squares: this study) is attributed to recharge of the pore water molybdate reservoir by the dissolution of Mn oxides (low δ^{98}Mo) and the diffusional transport of seawater molybdate (high δ^{98}Mo) into the sediment. (For interpretation of the references to color in this figure legend, the reader is referred to the web version of this article.)

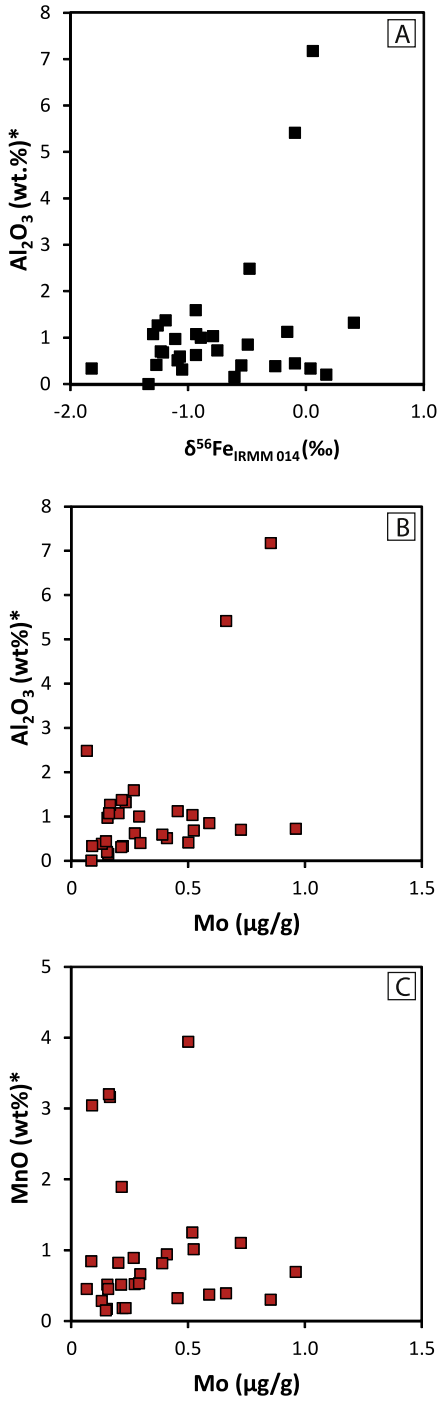

Fig. 4. (A) Compilation of δ^{56}Fe values and Al_2O_3* concentration data, which shows no correlation. (B) Compilation of Mo and Al_2O_3* concentration data, which also shows no correlation. This indicates that Mo enrichment is not associated with the supply of detrital material. (C) Similarly, there is no correlation between Mo and MnO* concentrations. Despite the linked flux of Mn oxides and adsorbed molybdate to the sediments, the final burial of Mo and Mn after dissolution of Mn oxides within the sediment might be decoupled (* indicates data from Nel, 2013).

5. Discussion

5.1. Iron isotopes

In modern redox stratified water bodies, free oxygen as well as Mn-oxide particle densities control Fe(II) oxidation to amorphous Fe-oxyhydroxides (Dellwig et al., 2010). These Fe-oxyhydroxide precipitates are isotopically heavy, leaving behind a $Fe(II)_{aq}$ reservoir with relatively lower δ^{56}Fe values (Johnson et al., 2008a). During the deposition of the Koegas iron formation the existence of a Mn oxide particle flux from the water column to the sediment has been demonstrated (J.E. Johnson et al., 2013). Therefore, the most straightforward explanation for the negative correlation between Mn concentrations and δ^{56}Fe values in the same chemical sediments observed here, is that Fe isotope fractionation within the water column is associated with Mn oxide formation. This interrelation is consistent with water column Fe isotope data for Lac Pavin in France, a modern redox-stratified lake which is claimed to be an "Archean ocean analogue" (Busigny et al., 2014). Similar to Precambrian oxygen oases, Lac Pavin shows an oxygenated upper surface layer separated from anoxic and ferruginous deep waters (Fig. 5). In such modern redox-stratified water columns, Mn(II) derived from anoxic deep waters is oxidized at a higher redox potential than Fe, i.e. above the Fe chemocline. The formation of Fe-oxyhydroxides is induced by the oxidation of upward diffusing Fe(II) by dissolved molecular oxygen and/or by the stepwise replacement of Mn(IV) by Fe(III) on sinking Mn-oxide particles (Dellwig et al., 2010). Partial oxidation of Fe(II) to Fe(III), and the concomitant enrichment of heavy Fe isotopes in precipitated Fe(III) minerals, leaves behind an $Fe(II)_{(aq)}$ reservoir with low δ^{56}Fe values (Fig. 5). This process is, thus, likely to generate a vertical isotopic gradient of dissolved Fe(II) and particulate Fe-oxyhydroxides along the redoxclines of stratified water columns. Accordingly, a sharp decline in δ^{56}Fe values of dissolved Fe(II) is observed in the Mn oxidation reaction zone of Lac Pavin (Busigny et al., 2014).

Although these trends in δ^{56}Fe values of dissolved $Fe(II)_{aq}$ are observed through the chemocline of Lac Pavin (Busigny et al., 2014), water column Fe isotope signatures are not preserved in the associated bulk rocks of the lake. One reason could be that the authigenic Fe isotope signatures from Lac Pavin were masked by detrital Fe, as indicated by lower Fe/Al ratios (<25) in the uppermost lake sediments (Schettler et al., 2007) compared to Kogeas Fe/Al ratios (between 30 and 346, excluding the shaly succession during interval 2; Table S1). The absence of a correlation between δ^{56}Fe values and Al_2O_3 concentrations in Koegas iron formations suggests that variations in δ^{56}Fe values were not caused by variable detrital contributions (Fig. 4A). More likely, however, the instantaneous and near quantitative oxidation of dissolved $Fe(II)_{aq}$ through a chemocline with a small vertical thickness impedes the preservation of resolvable authigenic water column Fe isotope signals in bulk sediments at Lac Pavin (Busigny et al., 2014). This instantaneous oxidation of $Fe(II)_{aq}$ in Lac Pavin might be emphasized by relatively slow diffusional upward transport of deep water $Fe(II)_{aq}$. In less restricted marine settings the occurrence of eddies and geostrophic currents would result in better vertical mixing of water bodies and the vertical extension of chemoclines (Zopfi et al., 2001). Within the Koegas basin, upwelling and the partial oxidation of deep water $Fe(II)_{aq}$ would cause the continuous depletion of heavy Fe isotopes in the remaining $Fe(II)_{aq}$ reservoir until the reservoir is exhausted in most proximal settings. Therefore, the δ^{56}Fe values of the Fe(II) pool would decrease towards the redox cline. The Fe oxides that precipitate from the more proximal Fe(II) pool, with relatively lower δ^{56}Fe values, should also show relatively lower δ^{56}Fe values.

Compared to modern marine basins, two additional parameters might have caused further vertical extension of the chemocline in Paleoproterozoic marine oxygen oases. First, the overall lower O_2 availability would have decreased abiotic $Mn(II)_{aq}$ and $Fe(II)_{aq}$ oxidation rates, because the half-life of $Mn(II)_{aq}$ and $Fe(II)_{aq}$ mainly depend on pH and the oxygen concentration in seawater (Field and Sherrell, 2000). Secondly, numerical models indicate that at low dissolved oxygen concentration the oxidation of Mn(II) rather than organic matter is the predominant O_2 consumer (Yakushev et al., 2007). The resultant formation of Mn(IV) particles, in turn,

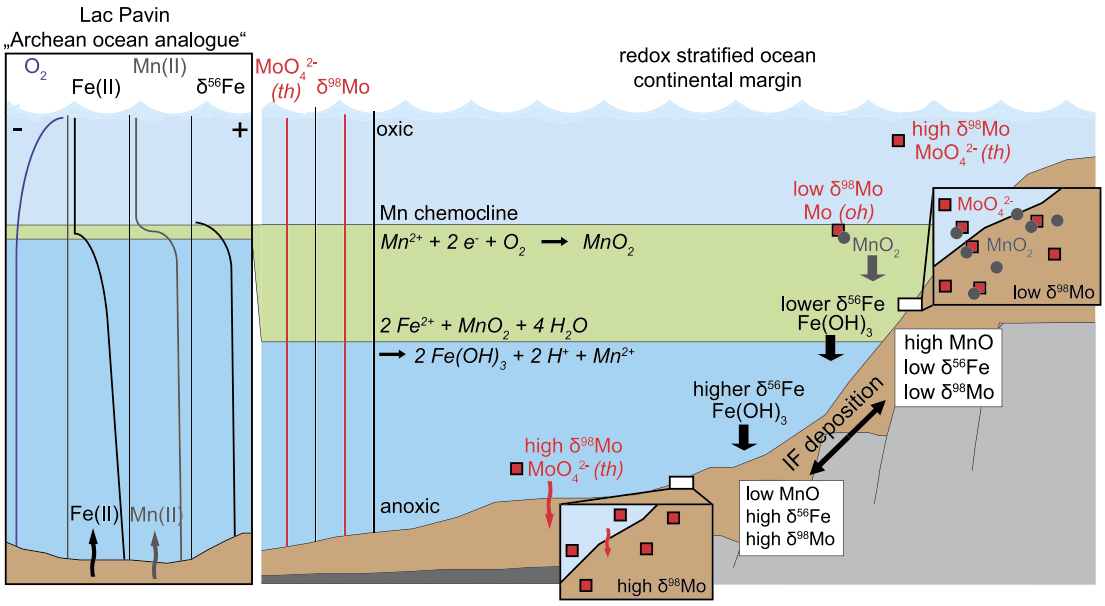

Fig. 5. The modeled environment during BIF deposition of the Koegas subgroup in comparison to Lac Pavin, an 'Archean ocean analogue' (Busigny et al., 2014). A chemocline divides anoxic deep waters from a well oxygenated surface layer. The upper water column is depleted in heavy Fe isotopes due to Fe(II) oxidation by Mn oxides. Fe oxides formed in shallower settings therefore show relatively lower δ^{56}Fe values. In respective settings the flux of Mn oxides is higher, which causes higher Mn(II) concentrations in the pore water (and carbonates). Bulk sediments, thus, show relatively high Mn concentrations. The preferential adsorption of isotopically light and octahedrally coordinated (*oh*) Mo onto these Mn oxides will cause lower δ^{98}Mo values in sediments from most proximal settings (Planavsky et al., 2014), where the flux of Mn oxides is highest. In more distal settings the diffusional transport of tetrahedrally coordinated (*th*) seawater Mo with higher δ^{98}Mo may be the predominant Mo source.

cause an increase in particle density and an acceleration of the rate of sinking. Altogether this increases the vertical extension of the chemocline in modern marine settings (Yakushev et al., 2007) and, thus, also the spatial resolution of water column Fe isotope signals within the sedimentary record. Consistent with recent modeling, the maintenance of very low oxygen concentrations in Archean oxygen oases is expected under a low O_2 atmosphere (Olson et al., 2013). We, therefore, suggest that shallow waters of the Griqualand West Basin were better mixed and distinctly lower in O_2 compared to Lac Pavin, causing non-quantitative Fe oxidation along a smooth chemocline.

Considering the mineralogy of GEC01 and GTF01 samples, high Mn abundances exclusively bound in carbonate phases imply the burial of Mn oxides and their quantitative reduction within the sediment (J.E. Johnson et al., 2013). The enrichment of Mn in secondary carbonates during diagenesis is controlled by pore water alkalinity and Mn availability, which largely depends on the flux of Mn oxides and organic matter to the sediment (Burdige, 1993; Lenz et al., 2015). The efficient reduction and re-dissolution of Mn oxides below the Mn redoxcline decreases the flux of Mn oxides to the sediment in the deeper parts of the anoxic basin (Dellwig et al., 2010; Tsikos et al., 2010). Relative enrichment of Mn in carbonates of GEC01 and GTF01 samples is therefore expected in sediments directly beneath the Mn chemocline, and in water depths with low δ^{56}Fe values of dissolved Fe(II) (Fig. 5). We suggest that this association causes the most negative δ^{56}Fe values in sediments with high Mn concentrations (Fig. 3A).

The preservation of distinct and primary trends in our dataset might have been aided by the paucity of Fe sulfides in our sample set (Nel, 2013), which strongly suggests that dissolved H_2S within the pore water was limited during the deposition of the Koegas Formation. This precludes iron isotope fractionation during pyrite formation. C.M. Johnson et al. (2013) argue that iron carbonates are unsuitable for the reconstruction of the redox structure of the water column, because of large Fe isotope fractionations during (bacterial) dissimilatory iron reduction within the sediment, which also affects the Fe isotopic composition of the reactive Fe(III) reservoir (Staubwasser et al., 2006). The differentiation between Fe isotope fractionations within the water column and the sediment, respectively, is therefore extremely difficult. However, Fe oxides in our samples are subordinate in abundance compared to Fe carbonates and Fe silicates (Nel, 2013). In analogy with the early diagenetic Mn(IV) reduction and Mn(II) carbonate formation, this might indicate a near quantitative reduction of primary Fe (oxy)hydroxides within the sediment and the exhaustion of the reactive Fe(III) reservoir, which would assure negligible net Fe isotope fractionations during dissimilatory iron reduction (Staubwasser et al., 2006). Assuming non-quantitative iron reduction during dissimilatory iron reduction in an open system, a back flux of isotopically light $Fe(II)_{aq}$ from pore waters to seawater would be expected. In modern anoxic settings like the Black Sea the lateral transport of this isotopically light $Fe(II)_{aq}$ towards the basin results in negative δ^{56}Fe values in basinal sediments (iron shuttle), whereas the residual shelf sediments become isotopically heavier (Severmann et al., 2008). However, the most proximal sediments with high Mn concentrations exhibit relatively lower δ^{56}Fe values, which argues against such a scenario for the Koegas sedimentary setting. We therefore suggest that upwelled $Fe(II)_{aq}$ from a ferruginous deep ocean gets depleted and isotopically light towards the chemocline. Qualitative variations in bulk sedimentary δ^{56}Fe values of Koegas samples reflect their relative position along an extended chemocline, with lowest δ^{56}Fe values in the most proximal sediments.

5.2. Molybdenum isotopes

The negative correlation of Mn concentrations and δ^{98}Mo values (Fig. 3B) has also been observed in other 1.8 to 3.0 Ga old iron formations (Planavsky et al., 2014). Planavsky et al. (2014) suggested that low δ^{98}Mo values reflect the local formation of Mn oxides and the subsequent preferential adsorption of isotopically light Mo resulting in Mn enriched samples having the lowest δ^{98}Mo values. As mentioned above, Mn oxides were quantitatively reduced within the sediment (J.E. Johnson et al., 2013), which also causes the re-liberation of adsorbed Mo (Scott and Lyons, 2012). Carbonates represent the predominant final sedimentary host for both Mn and Mo (J.E. Johnson et al., 2013;

Planavsky et al., 2014). However, their partitioning behavior into carbonates might be different. Moreover, re-liberated pore water Mn and Mo are expected to exchange with the overlying water column. Thereby, the diffusional gradient is mainly controlled by the Mo and Mn concentration gradients between the bottom seawater and the pore water, respectively. The extent of exchange of Mo and Mn with the overlying water masses might also have caused the decoupling of bulk sedimentary Mo and Mn concentrations. This is documented in the absence of a correlation between Mo and Mn concentration (Fig. 4). The Mo isotope data seems more robust against this decoupling. Due to insignificant Mo isotope fractionation during the incorporation of Mo in precipitated abiogenic carbonates (Voegelin et al., 2010), the bulk Mo isotopic composition depends on the pore water Mo isotopic composition. We suggest that this pore water molybdate reservoir is recharged by the dissolution of Mn oxides (low δ^{98}Mo) as well as the diffusional transport of seawater molybdate (high δ^{98}Mo) into the sediment. The higher the flux of Mn oxides to the sediments, the more relevant is the isotopically light component of adsorbed Mo for the pore water molybdate reservoir (Fig. 5).

Next to Mn oxides, adsorption of Mo onto Fe-(hydr)oxide phases has been suggested as another possible mechanism to preferentially remove isotopically light Mo (Czaja et al., 2012; Goldberg et al., 2009). As modeled by Czaja et al. (2012) such a removal pathway should result in a negative correlation between Mo and Fe isotopes. However, Koegas samples show a positive correlation between Fe and Mo isotopes, which has also been observed in other iron formations (Planavsky et al., 2014). Furthermore, significantly lower Mo adsorption coefficients were determined for ferrihydrite compared to Mn oxides (Kashiwabara et al., 2011). Altogether these observations seem more consistent with the more recent suggestion that this sequestration pathway was relatively unimportant in Archean and Paleoproterozoic times (Kurzweil et al., 2015).

The local formation of Mn oxides within the water column of the Griqualand West Basin is consistent with our Fe isotope results as well as mineralogical observations (J.E. Johnson et al., 2013). The negative correlation of δ^{98}Mo values and Mn concentrations in our sample set therefore supports the interpretation of Planavsky et al. (2014) of precursor Mn-oxides in the sediment, which preferentially adsorbed light Mo isotopes. But the question arises of whether the particle shuttle and the subsequent transportation of isotopically light Mo within extended chemoclines were capable of influencing the concentration, distribution and the isotopic composition of dissolved molybdate in the water column. Such a relation has been discussed for other dissolved elements (e.g. silicon and phosphorous), which might have been similarly affected by particle adsorption processes (Fischer and Knoll, 2009). Assuming a very small seawater molybdate reservoir, efficient Mo drawdown by adsorption onto Mn oxides might have affected the local dissolved molybdate reservoir, similar to the Fe(II) reservoir. In this case the preferential adsorption of isotopically light molybdate onto Mn oxides would leave behind an uppermost water column that is isotopically heavy. If such a change in the water column Mo isotopic composition was the primary factor controlling the sedimentary δ^{98}Mo value (in analog to our Fe), high δ^{98}Mo values should correlate with high Mn concentrations and low δ^{56}Fe values, which is not the case. Instead, if the removal of Mo by adsorption onto Mn oxides had a minor effect on the concentration and the isotopic composition of the local seawater molybdate reservoir, lower δ^{98}Mo values in most proximal sediments with high fluxes of Mn oxides (and adsorbed isotopically light Mo) would be expected (Fig. 5). Our data, therefore, suggest an at least regionally homogeneous seawater Mo isotopic composition and a significant Mo seawater reservoir in the oxic surface layer and beyond the deeper ferruginous ocean at the time of Koegas sedimentation (Fig. 5).

5.3. Summary and implications for the Pre-GOE environment

Our data strongly suggest a stratified water column in the Griqualand West Basin around 2.48 Ga ago shortly before the GOE, with a continuous smooth chemocline between slightly oxic shallow waters and ferruginous deep waters. The precise local burial pathways of Fe and Mo within such an oxygen oasis are different but are both related to the formation of Mn oxides along the redox boundary. The oxidation of $Fe(II)_{aq}$ along the Mn redox-cline causes a shift in the δ^{56}Fe value of the local water column, as also observed in modern redox-stratified lakes. The concentration and isotopic composition of dissolved Fe reservoirs is substantially affected by the redox shuttling of Fe and Mn. In contrast, the removal of isotopically light Mo during adsorption onto Mn oxides seems to have a negligible effect on the Mo reservoir and the local seawater δ^{98}Mo value down the water column (Fig. 5). Sedimentary Mo isotope measurements, therefore, have the general potential to trace regional or even global redox changes independent of their depositional depth. However, the early diagenetic Mn-oxidation–reduction cycle within the sediment, exchange rates with the overlying water column Mo reservoir, and the non-quantitative Mo scavenging from pore fluids into secondary carbonates, make iron formations an inadequate sedimentary deposit to reconstruct the regional or global seawater Mo isotopic composition and its variation with time (in contrast to black shales and iron formations with no Mn cycling (Kurzweil et al., 2015)).

If δ^{56}Fe values, δ^{98}Mo values and Mn concentrations depend on the proximity to the oxic–anoxic redox boundary, their temporal variation might be a consequence of sea level fluctuations. Relatively high δ^{56}Fe values, high δ^{98}Mo values and low Mn concentrations reflect a sea level high stand. Consistent with this hypothesis, a transgressive event at the base of the Nelani Formation (Beukes, 1983) coincides with an increase in δ^{98}Mo values and δ^{56}Fe values and lower Mn concentrations. The subsequent regression during the Nelani Formation is accompanied by decreasing δ^{56}Fe values and higher Mn concentrations. This close relationship of δ^{56}Fe values and Mn concentrations may also provide indications for iron formation deposition in general, considering the debate over biotic vs. abiotic induced iron formation deposition (Drever, 1974; Holland, 2006; Kappler et al., 2005; Widdel et al., 1993). In principle, Mn and Fe oxide formation could be decoupled but coincide in time. More straightforward, however, seems the suggestion that, at least for Koegas iron formations, the precipitation of Fe(III) minerals is mainly related to abiotic Fe(II) oxidation by Mn oxides along the Mn redox boundary. It remains, however, unclear if Mn oxidation, in turn, is linked to Mn oxidizing bacteria (J.E. Johnson et al., 2013) or O_2 production by oxygenic photosynthesis (Planavsky et al., 2014).

Acknowledgements

Brian Philip Nel is acknowledged for the detailed petrological, chemical and mineralogical description of the sample material, which was compiled during his dissertation. We further thank the German Research Foundation (grants WI3870/2-1) and the Carl Zeiss Foundation for financial support for this project. Funding for the two drill cores was provided by the Agouron Institute, Pesadena, California, USA. We thank Noah Planavsky and two anonymous reviewers for constructive and helpful reviews and Derek Vance for the editorial handling of the manuscript.

Appendix A. Supplementary material

Supplementary material related to this article can be found online at http://dx.doi.org/10.1016/j.epsl.2016.07.013.

References

Barling, J., Anbar, A., 2004. Molybdenum isotope fractionation during adsorption by manganese oxides. Earth Planet. Sci. Lett. 217, 315–329.

Beard, B.L., Johnson, C.M., 2004. Fe isotope variations in the modern and ancient earth and other planetary bodies. Rev. Mineral. Geochem. 55, 319–357.

Beard, B.L., Johnson, C.M., Von Damm, K.L., Poulson, R.L., 2003. Iron isotope constraints on Fe cycling and mass balance in oxygenated Earth oceans. Geology 31, 629–632.

Bertine, K.K., Turekian, K.K., 1973. Molybdenum in marine deposits. Geochim. Cosmochim. Acta 37, 1415–1434.

Beukes, N., 1983. Palaeoenvironmental setting of iron-formations in the depositional basin of the Transvaal Supergroup, South Africa. Dev. Precambrian Geol. 6, 131–198.

Beukes, N.J., Gutzmer, J., 2008. Origin and paleoenvironmental significance of major iron formations at the Archean–Paleoproterozoic boundary. Rev. Econ. Geol. 15, 5–47.

Burdige, D.J., 1993. The biogeochemistry of manganese and iron reduction in marine sediments. Earth-Sci. Rev. 35, 249–284.

Busigny, V., Planavsky, N.J., Jézéquel, D., Crowe, S., Louvat, P., Moureau, J., Viollier, E., Lyons, T.W., 2014. Iron isotopes in an Archean ocean analogue. Geochim. Cosmochim. Acta 133, 443–462.

Catling, D.C., Zahnle, K.J., McKay, C.P., 2001. Biogenic methane, hydrogen escape, and the irreversible oxidation of early Earth. Science 293, 839–843.

Croal, L.R., Johnson, C.M., Beard, B.L., Newman, D.K., 2004. Iron isotope fractionation by Fe(II)-oxidizing photoautotrophic bacteria. Geochim. Cosmochim. Acta 68, 1227–1242.

Czaja, A.D., Johnson, C.M., Roden, E.E., Beard, B.L., Voegelin, A.R., Nägler, T.F., Beukes, N.J., Wille, M., 2012. Evidence for free oxygen in the Neoarchean ocean based on coupled iron–molybdenum isotope fractionation. Geochim. Cosmochim. Acta 86, 118–137.

Dauphas, N., Rouxel, O., 2006. Mass spectrometry and natural variations of iron isotopes. Mass Spectrom. Rev. 25, 515–550.

de Laeter, J.R., Böhlke, J.K., De Bièvre, P., Hidaka, H., Peiser, H., Rosman, K., Taylor, P., 2003. Atomic weights of the elements. Review 2000 (IUPAC Technical Report). Pure Appl. Chem. 75, 683–800.

Dellwig, O., Leipe, T., März, C., Glockzin, M., Pollehne, F., Schnetger, B., Yakushev, E.V., Böttcher, M.E., Brumsack, H.-J., 2010. A new particulate Mn–Fe–P-shuttle at the redoxcline of anoxic basins. Geochim. Cosmochim. Acta 74, 7100–7115.

Drever, J.I., 1974. Geochemical model for the origin of Precambrian banded iron formations. Geol. Soc. Am. Bull. 85, 1099–1106.

Farquhar, J., Bao, H., Thiemens, M., 2000. Atmospheric influence of Earth's earliest sulfur cycle. Science 289, 756–758.

Field, M.P., Sherrell, R.M., 2000. Dissolved and particulate Fe in a hydrothermal plume at 9°45′N, East Pacific Rise: slow Fe(II) oxidation kinetics in Pacific plumes. Geochim. Cosmochim. Acta 64, 619–628.

Fischer, W.W., Knoll, A.H., 2009. An iron shuttle for deepwater silica in Late Archean and early Paleoproterozoic iron formation. Geol. Soc. Am. Bull. 121, 222–235.

Goldberg, T., Archer, C., Vance, D., Poulton, S.W., 2009. Mo isotope fractionation during adsorption to Fe (oxyhydr)oxides. Geochim. Cosmochim. Acta 73, 6502–6516.

Goldberg, T., Gordon, G., Izon, G., Archer, C., Pearce, C.R., McManus, J., Anbar, A.D., Rehkämper, M., 2013. Resolution of inter-laboratory discrepancies in Mo isotope data: an intercalibration. J. Anal. At. Spectrom. 28, 724–735.

Greber, N.D., Siebert, C., Nägler, T.F., Pettke, T., 2012. δ98/95Mo values and molybdenum concentration data for NIST SRM 610, 612 and 3134: towards a common protocol for reporting Mo data. Geostand. Geoanal. Res. 36, 291–300.

Holland, H.D., 2006. The oxygenation of the atmosphere and oceans. Philos. Trans. R. Soc. Lond. B, Biol. Sci. 361, 903–915.

Johnson, C.M., Beard, B.L., Klein, C., Beukes, N.J., Roden, E.E., 2008a. Iron isotopes constrain biologic and abiologic processes in banded iron formation genesis. Geochim. Cosmochim. Acta 72, 151–169.

Johnson, C.M., Beard, B.L., Roden, E.E., 2008b. The iron isotope fingerprints of redox and biogeochemical cycling in modern and ancient Earth. Annu. Rev. Earth Planet. Sci. 36, 457–493.

Johnson, C.M., Ludois, J.M., Beard, B.L., Beukes, N.J., Heimann, A., 2013. Iron formation carbonates: paleoceanographic proxy or recorder of microbial diagenesis? Geology 41, 1147–1150.

Johnson, J.E., Webb, S.M., Thomas, K., Ono, S., Kirschvink, J.L., Fischer, W.W., 2013. Manganese-oxidizing photosynthesis before the rise of cyanobacteria. Proc. Natl. Acad. Sci. USA 110, 11238–11243.

Kappler, A., Pasquero, C., Konhauser, K.O., Newman, D.K., 2005. Deposition of banded iron formations by anoxygenic phototrophic Fe(II)-oxidizing bacteria. Geology 33, 865–868.

Kashiwabara, T., Takahashi, Y., Tanimizu, M., Usui, A., 2011. Molecular-scale mechanisms of distribution and isotopic fractionation of molybdenum between seawater and ferromanganese oxides. Geochim. Cosmochim. Acta 75, 5762–5784.

Kaufman, A.J., Johnston, D.T., Farquhar, J., Masterson, A.L., Lyons, T.W., Bates, S., Anbar, A.D., Arnold, G.L., Garvin, J., Buick, R., 2007. Late Archean biospheric oxygenation and atmospheric evolution. Science 317, 1900–1903.

Kendall, B., Reinhard, C.T., Lyons, T.W., Kaufman, A.J., Poulton, S.W., Anbar, A.D., 2010. Pervasive oxygenation along late Archaean ocean margins. Nat. Geosci. 3, 647–652.

Kendall, B., van Acken, D., Creaser, R.A., 2013. Depositional age of the early Paleoproterozoic Klipputs Member, Nelani Formation (Ghaap Group, Transvaal Supergroup, South Africa) and implications for low-level Re–Os geochronology and Paleoproterozoic global correlations. Precambrian Res. 237, 1–12.

Kump, L.R., Barley, M.E., 2007. Increased subaerial volcanism and the rise of atmospheric oxygen 2.5 billion years ago. Nature 448, 1033–1036.

Kurzweil, F., Claire, M., Thomazo, C., Peters, M., Hannington, M., Strauss, H., 2013. Atmospheric sulfur rearrangement 2.7 billion years ago: evidence for oxygenic photosynthesis. Earth Planet. Sci. Lett. 366, 17–26.

Kurzweil, F., Wille, M., Schoenberg, R., Taubald, H., Van Kranendonk, M.J., 2015. Continuously increasing δ^{98}Mo values in Neoarchean black shales and iron formations from the Hamersley Basin. Geochim. Cosmochim. Acta 164, 523–542.

Learman, D.R., Voelker, B.M., Madden, A.S., Hansel, C.M., 2013. Constraints on superoxide mediated formation of manganese oxides. Front. Microbiol. 4, 262.

Lehmann, B., Nägler, T.F., Holland, H.D., Wille, M., Mao, J., Pan, J., Ma, D., Dulski, P., 2007. Highly metalliferous carbonaceous shale and Early Cambrian seawater. Geology 35, 403–406.

Lenz, C., Jilbert, T., Conley, D., Wolthers, M., Slomp, C., 2015. Are recent changes in sediment manganese sequestration in the euxinic basins of the Baltic Sea linked to the expansion of hypoxia? Biogeosciences 12, 4875–4894.

Lyons, T.W., Reinhard, C.T., Planavsky, N.J., 2014. The rise of oxygen in Earth's early ocean and atmosphere. Nature 506, 307–315.

Miller, C.A., Peucker-Ehrenbrink, B., Walker, B.D., Marcantonio, F., 2011. Re-assessing the surface cycling of molybdenum and rhenium. Geochim. Cosmochim. Acta 75, 7146–7179.

Moeller, K., Schoenberg, R., Grenne, T., Thorseth, I.H., Drost, K., Pedersen, R.B., 2014. Comparison of iron isotope variations in modern and Ordovician siliceous Fe oxyhydroxide deposits. Geochim. Cosmochim. Acta 126, 422–440.

Nägler, T.F., Anbar, A.D., Archer, C., Goldberg, T., Gordon, G.W., Greber, N.D., Siebert, C., Sohrin, Y., Vance, D., 2014. Proposal for an international molybdenum isotope measurement standard and data representation. Geostand. Geoanal. Res. 38, 149–151.

Nakagawa, Y., Takano, S., Firdaus, M.L., Norisuye, K., Hirata, T., Vance, D., Sohrin, Y., 2012. The molybdenum isotopic composition of the modern ocean. Geochem. J. 46, 131–141.

Nel, B.P., 2013. Petrography and Geochemistry of Iron Formations of the Paleoproterozoic Koegas Subgroup, Transvaal Supergroup, Griqualand West, South Africa. University of Johannesburg, p. 134.

Olson, S.L., Kump, L.R., Kasting, J.F., 2013. Quantifying the areal extent and dissolved oxygen concentrations of Archean oxygen oases. Chem. Geol. 362, 35–43.

Pavlov, A., Kasting, J., 2002. Mass-independent fractionation of sulfur isotopes in Archean sediments: strong evidence for an anoxic Archean atmosphere. Astrobiology 2, 27–41.

Pickard, A., 2003. SHRIMP U–Pb zircon ages for the Palaeoproterozoic Kuruman Iron Formation, Northern Cape Province, South Africa: evidence for simultaneous BIF deposition on Kaapvaal and Pilbara Cratons. Precambrian Res. 125, 275–315.

Planavsky, N.J., Asael, D., Hofmann, A., Reinhard, C.T., Lalonde, S.V., Knudsen, A., Wang, X., Ossa, F.O., Pecoits, E., Smith, A.J., 2014. Evidence for oxygenic photosynthesis half a billion years before the Great Oxidation Event. Nat. Geosci. 7, 283–286.

Rouxel, O.J., Bekker, A., Edwards, K.J., 2005. Iron isotope constraints on the Archean and Paleoproterozoic ocean redox state. Science 307, 1088–1091.

Schettler, G., Schwab, M.J., Stebich, M., 2007. A 700-year record of climate change based on geochemical and palynological data from varved sediments (Lac Pavin, France). Chem. Geol. 240, 11–35.

Schoenberg, R., von Blanckenburg, F., 2005. An assessment of the accuracy of stable Fe isotope ratio measurements on samples with organic and inorganic matrices by high-resolution multicollector ICP-MS. Int. J. Mass Spectrom. 242, 257–272.

Schröder, S., Bedorf, D., Beukes, N., Gutzmer, J., 2011. From BIF to red beds: sedimentology and sequence stratigraphy of the Paleoproterozoic Koegas Subgroup (South Africa). Sediment. Geol. 236, 25–44.

Scott, C., Lyons, T.W., 2012. Contrasting molybdenum cycling and isotopic properties in euxinic versus non-euxinic sediments and sedimentary rocks: refining the paleoproxies. Chem. Geol. 324, 19–27.

Severmann, S., Lyons, T.W., Anbar, A., McManus, J., Gordon, G., 2008. Modern iron isotope perspective on the benthic iron shuttle and the redox evolution of ancient oceans. Geology 36, 487–490.

Siebert, C., Nägler, T.F., von Blanckenburg, F., Kramers, J.D., 2003. Molybdenum isotope records as a potential new proxy for paleoceanography. Earth Planet. Sci. Lett. 211, 159–171.

Staubwasser, M., Von Blanckenburg, F., Schoenberg, R., 2006. Iron isotopes in the early marine diagenetic iron cycle. Geology 34, 629–632.

Tebo, B.M., Johnson, H.A., McCarthy, J.K., Templeton, A.S., 2005. Geomicrobiology of manganese(II) oxidation. Trends Microbiol. 13, 421–428.

Tsikos, H., Matthews, A., Erel, Y., Moore, J.M., 2010. Iron isotopes constrain biogeochemical redox cycling of iron and manganese in a Palaeoproterozoic stratified basin. Earth Planet. Sci. Lett. 298, 125–134.

Voegelin, A.R., Nägler, T.F., Beukes, N.J., Lacassie, J.P., 2010. Molybdenum isotopes in late Archean carbonate rocks: implications for early Earth oxygenation. Precambrian Res. 182, 70–82.

Voegelin, A.R., Pettke, T., Greber, N.D., von Niederhäusern, B., Nägler, T.F., 2014. Magma differentiation fractionates Mo isotope ratios: evidence from the Kos Plateau Tuff (Aegean Arc). Lithos 190, 440–448.

Welch, S., Beard, B., Johnson, C., Braterman, P., 2003. Kinetic and equilibrium Fe isotope fractionation between aqueous Fe(II) and Fe(III). Geochim. Cosmochim. Acta 67, 4231–4250.

Weyer, S., Schwieters, J., 2003. High precision Fe isotope measurements with high mass resolution MC-ICPMS. Int. J. Mass Spectrom. 226, 355–368.

Widdel, F., Schnell, S., Heising, S., Ehrenreich, A., Assmus, B., Schink, B., 1993. Ferrous iron oxidation by anoxygenic phototrophic bacteria. Nature 362, 834–836.

Yakushev, E., Pollehne, F., Jost, G., Kuznetsov, I., Schneider, B., Umlauf, L., 2007. Analysis of the water column oxic/anoxic interface in the Black and Baltic seas with a numerical model. Mar. Chem. 107, 388–410.

Zopfi, J., Ferdelman, T.G., Jørgensen, B.B., Teske, A., Thamdrup, B., 2001. Influence of water column dynamics on sulfide oxidation and other major biogeochemical processes in the chemocline of Mariager Fjord (Denmark). Mar. Chem. 74, 29–51.